1    **Structure Determination of Inactive-State GPCRs with a Universal Nanobody**

2

3    Michael J. Robertson[1,2], Makaía Papasergi-Scott[1,2], Feng He[1,2], Alpay B. Seven[1,2], Justin

4    G. Meyerowitz[1,2,3], Ouliana Panova[1,2], Maria Claudia Peroto[1,2], Tao Che[4,5], Georgios

5    Skiniotis[1,2,6]

6

7    [1]Department of Molecular and Cellular Physiology, Stanford University School of

8    Medicine, Stanford, CA, USA

9    [2]Department of Structural Biology, Stanford University School of Medicine, Stanford, CA,

10   USA

11   [3]Department of Anesthesiology, Perioperative and Pain Medicine, Stanford University

12   School of Medicine, Stanford, CA 94305, USA

13   [4]Department of Anesthesiology, Washington University School of Medicine, St. Louis,

14   Missouri, 63110, USA

15   [5]Center for Clinical Pharmacology, University of Health Sciences & Pharmacy at St. Louis

16   and Washington University School of Medicine, St. Louis, Missouri, 63110, USA

17   [6]Correspondence: yiorgo@stanford.edu

18

19   **Summary**

20   Cryogenic electron microscopy (cryo-EM) has widened the field of structure-based drug

21   discovery by allowing for routine determination of membrane protein structures previously

22   intractable. However, despite representing one of the largest classes of therapeutic

23   targets, most inactive-state G protein-coupled receptors (GPCRs) have remained

24 inaccessible for cryo-EM because their small size and membrane-embedded nature

25 impedes projection alignment for high-resolution map reconstructions. Here we

26 demonstrate that the same single-chain camelid antibody (nanobody) recognizing a

27 grafted intracellular loop can be used to obtain cryo-EM structures of different inactive-

28 state GPCRs at resolutions comparable or better than those obtained by X-ray

29 crystallography. Using this approach, we obtained the structure of human neurotensin 1

30 receptor (NTSR1) bound to antagonist SR48692, of μ-opioid receptor (MOR) bound to

31 the clinical antagonist alvimopan, as well as the structures of the previously

32 uncharacterized somatostatin receptor 2 (SSTR2) in the apo state and histamine receptor

33 2 (H2R) bound to the H2 blocker famotidine. Each of these structures yields novel insights

34 into ligand binding and specificity. We expect this rapid, straightforward approach to

35 facilitate the broad structural exploration of GPCR inactive states without the need for

36 extensive engineering and crystallization.

37

38 **Introduction**

39     The impact of cryo-EM on structure-based drug discovery has been immense,

40 leading to the characterization of a wide variety of new and valuable membrane protein

41 drug targets, including ion channels and G protein-coupled receptors (GPCRs)[1]. As a key

42 requirement for high-resolution cryo-EM map reconstructions, the randomly oriented

43 particle projections must first be correctly aligned at intermediate-to-low resolution, a step

44 that often fails for small proteins due to their limited structural features. For relatively small

45 membrane proteins, the problem is compounded by the presence of a detergent micelle

46 or lipid nanodisc used for solubilization, which further dampens the contrast of embedded

47 protein densities. These obstacles pose a major bottleneck for cryo-EM structure

48 determination of GCPRs, which account for roughly 35% of FDA-approved drugs.

49 Approximately half of those are agonists that activate the receptor and the other half

50 antagonists or inverse agonists[2] that engage the inactive-state receptor, thereby blocking

51 endogenous signaling. Active-state GPCR structures have been obtained by cryo-EM in

52 complex with heterotrimeric G protein[3], a ~90 kDa entity that adds significant mass

53 outside the detergent micelle or lipid disc and provides a source of alignment for the

54 transmembrane receptor. However, there is no such generalizable tool for cryo-EM

55 structure determination of inactive-state GPCRs, especially for family A receptors, the

56 largest GCPR subfamily with hundreds of receptors that are typically ~37-50 kDa and lack

57 sizeable extracellular domains for projection alignment. Thus, the application of cryo-EM

58 is severely limited for inactive-state GPCRs, and their structural elucidation mostly relies

59 on extensive engineering and crystallization trials for X-ray studies. This limitation impacts

60 mechanistic investigations of GPCRs and structure-based drug discovery for the

61 countless therapeutically relevant receptors.

62 Che *et al.*[4] recently reported a camelid VHH domain antibody, referred to as

63 nanobody 6 (Nb6), that engages the inactive-state intracellular loop 3 (ICL3) of the κ-

64 opioid receptor (KOR), even when this loop is grafted onto a wide range of receptors,

65 including orphan receptors and family B receptors. This tool was initially developed as a

66 bioluminescence resonance energy transfer (BRET)-based sensor of receptor activation

67 state, an approach that also allows for cost-effective and robust screening of Nb6-binding

68 constructs by employing BRET assays. Using the Nb6 approach, we obtained three-

69 dimensional (3D) map reconstructions of human NTSR1 (hNTSR1) in complex with Nb6

70    bound to the inverse agonist SR48692[5] at a resolution of 2.4 Å; the mouse MOR bound

71    to a megabody[6], an enlarged nanobody construct derived from Nb6 (Mb6), in complex

72    with the antagonist alvimopan[7] at a resolution of 2.8 Å; and the unliganded (apo) structure

73    of human SSTR2 bound to Nb6 at 3.1 Å resolution. Further, a modified Nb6 (Nb6M) was

74    cloned by grafting antigen-binding loops onto an alpaca nanobody scaffold and coupled

75    with a nanobody-binding antibody fragment (NabFab[8]) to determine the structure of

76    histamine receptor 2 (H2R) bound to famotidine at 3.0 Å resolution. Through these four

77    structures, we demonstrate that Nb6 is a general solution for determining high-resolution

78    inactive-state GPCRs by cryo-EM. Besides alleviating the need for extensive construct

79    engineering and crystallogenesis, the cryo-EM/Nb6 approach has two distinct

80    advantages: first, it does not necessitate the screening and development of receptor-

81    specific nanobodies. Second, the Nb6 BRET-based sensor allows for rapid and efficient

82    screening of constructs and conditions instead of time-consuming and expensive cryo-

83    EM-based screening.

84

85    **Employing Nb6 for cryo-EM structure determination of GPCRs**

86        Any fiducial marker used for cryo-EM structure determination of a target

87    macromolecule needs to be rigid in its binding and orientation in respect to the structural

88    target. Furthermore, if the marker is particularly small related to the target, it must be

89    positioned to provide a distinct feature from various angles to allow unambiguous

90    alignment of the randomly-oriented cryo-EM projections. A crystal structure of Nb6 bound

91    to KOR revealed an interaction at the base of TM5 and TM6, off-center from the major

92    axis of the receptor[4]. We hypothesized that this type of interaction would be an ideal

93     asymmetric fiduciary for cryo-EM particle projection alignment as it would allow for the

94     determination of the rotational orientation of the receptor around its major axis, particularly

95     during initial low-resolution alignments.

96          To evaluate the degree of rigidity of Nb6 when bound to a GPCR, we first

97     performed all-atom molecular dynamics (MD) simulations using the crystal structure of

98     the KOR-Nb6 complex. Alignment of the MD trajectories on the receptor atoms and

99     calculation of the average root mean squared fluctuation (RMSF) for Nb6 atoms over the

100    final 100 ns of triplicate 500 ns simulations (Fig. 1a) showed that Nb6 is rigidly bound and

101    characterized by little flexibility, except for the distal loops at the base of the nanobody.

102         Encouraged by these computational predictions, we employed Nb6 for *de novo*

103    cryo-EM structure determination of four pharmacologically relevant family A GPCRs. The

104    first, NTSR1, is broadly associated with neurological and gastrointestinal processes[9].

105    Overexpression of NTSR1 in some tumor types promotes cancer progression and

106    metastasis and is thus associated with poor prognosis[10], prompting the study and

107    development of NTSR1 inverse agonists for oncology[11]. We also studied MOR, the target

108    of opioids, which are both the most effective treatment for pain and also the therapeutic

109    class underlying the ongoing opioid epidemic in the United States[12]. While current opioid

110    antagonists can treat acute opioid overdose, there is an urgent need for MOR antagonists

111    with improved pharmacokinetic properties[12,13]. SSTR2 plays a pivotal role in the

112    neuroendocrine system by opposing the release of many hormones, including growth

113    hormone[14]. SSTR agonists are commonly prescribed for neuroendocrine tumors, while

114    SSTR subtype-selective antagonists are in development for diabetes, but the lack of

115    structural information for any somatostatin receptor family member in either active or

116    inactive state has made the development of next-generation SSTR ligands challenging.

117    Finally, selective H2R antagonists have a long history of clinical usage for peptic ulcers

118    and gastroesophageal reflux disease and are amongst the most prescribed drugs.

119    However, only structures of histamine receptor 1, the target for commonly prescribed

120    drugs for allergic rhinitis and other allergies, have been determined to date, impeding a

121    full understanding of histamine receptor subtype selectivity.

122        As originally described in Che *et al.*, we engineered constructs to enable binding

123    of Nb6 to mouse MOR and human SSTR2 by identifying minimal swaps of ICL3 along

124    with the cytoplasmic tips of transmembrane helix 5 and 6 (TM5/6) with that of the KOR

125    (Fig. 1c). In the case of the closely related MOR, the two point mutations M264L and

126    K269$^{6.24}$R (Ballesteros-Weinstein notation[15]; Fig. 1c) were sufficient to enable Nb6

127    binding. SSTR2 was able to bind Nb6 with the swap of all 15 residues from S238$^{5.68}$ of

128    TM5 (V256$^{5.68}$ of KOR) to K252$^{6.31}$ of TM6 (R270$^{6.31}$ of KOR) (Fig. 1c). For human NTSR1

129    (hNTSR1) we utilized the same swap from KOR T247$^{5.59}$ to L277$^{6.38}$ as previously

130    described for rat NTSR1[4] (rNTSR1; Fig. 1c). Similarly, for human H2R we used an

131    identical hybrid as described in Che *et al.* (KOR V244$^{5.56}$ to V285$^{6.46}$, Fig 1c). Notably,

132    BRET assays of agonist-induced Nb6 dissociation confirmed construct functionality, with

133    all four receptors showing dissociation of the nanobody in response to agonist binding

134    (Fig. 1d-g). In all experimental replicates, the BRET data for MOR response to DAMGO

135    appears to be biphasic, consistent with prior nanobody-based MOR activation sensors[16],

136    where distinct plasma membrane and endosomal signaling results in a two-phase
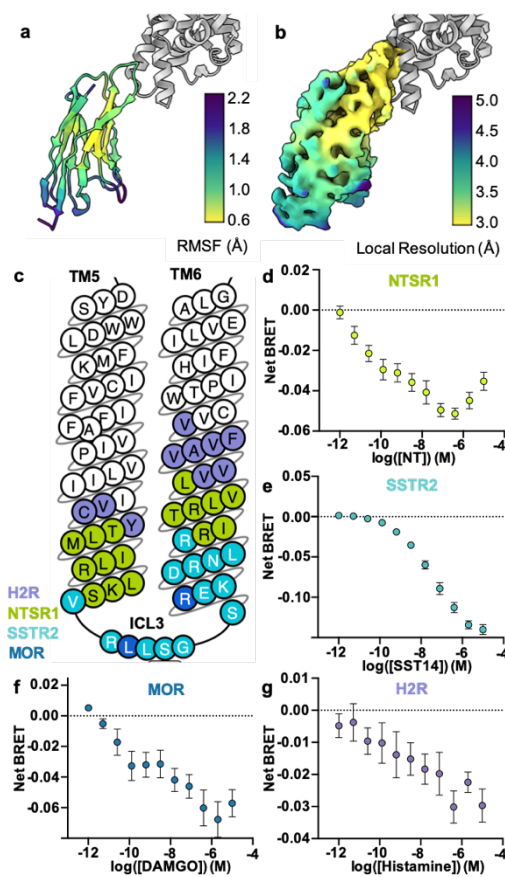
137    response.

**Fig 1. Construct design & evaluation for inactive state GPCR structure determination**
**a,** Root mean squared fluctuations (RMSF) in atomic positions overaged over triplicate molecular dynamics simulations for Nb6 bound to KOR. **b,** local resolution plot of Nb6 from the SSTR2/Nb6 complex cryoEM map. **c,** overlay of the three KOR ICL3 constructs used to enable Nb6 binding for MOR (two point mutations), SSTR2 (5.68 to 6.31), and hNTSR1 (5.59 to 6.38). Dose-response curves representing loss of BRET transfer (net BRET) between Receptor-rLuc and Nb6-mVenus for **d,** NTSR1$_K$ and neurotensin (NT), **e,** MOR$_K$ and DAMGO, **f,** SSTR2$_K$ and SST14, and **g,** H2R$_K$ and histamine.

High-resolution cryo-EM structure determination was feasible in all cases. Despite Nb6 being only 12 kDa, Nb6, or the equivalent region of Mb6, is resolved in three maps, providing a critical stable density outside the detergent micelle surrounding NSTR1, MOR and SSTR2. Notably, the local resolution indications for Nb6 in our GPCR/Nb6 complex cryo-EM maps showed a high correlation with the relative root mean square fluctuation (RMSF) values for Nb6 calculated from our MD simulations (Fig. 1c). This observation further demonstrates the strong predictive power of MD simulations in assessing the behavior of fiducial markers for such work. In the case of H2R/Nb6M/NabFab, the entire complex is fairly rigid and well resolved, due, in part, to the nanobody modifications and/or the binding of the NabFab rigidifying the loops of Nb6M.

## Structure of hNTSR1

149

150        Obtaining inactive-state crystal structures has proven challenging for NTSR1. The

151    only available crystal structures were determined in 2021[17]: one with a receptor in the apo

152    state (3.19 Å) and several structures with the receptor bound to the inverse agonists
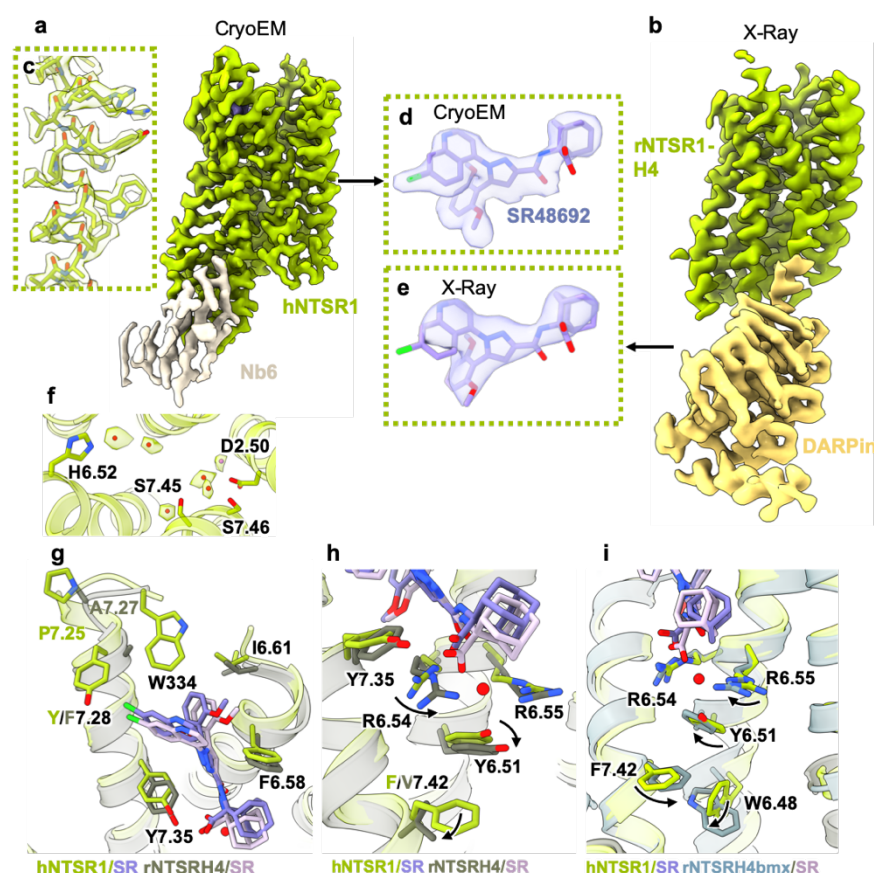


**Fig 2. Comparison of cryoEM structure of hNTSR1 and crystal structure of rNTSR1-H4 and rNTSR1-H4bmx**

**a,** 2.4 Å global resolution cryoEM map of hNTSR1. **b,** 2Fo-Fc crystallography map at 2.6 Å of rNTSR-H4 contoured at $\sigma$=1.0. **c,** hNTSR1 TM5 with cryoEM map **d,** Local EM map around bound inverse agonist SR48692. **e,** Local 2Fo-Fc map around SR48692 contoured at $\sigma$=1.25. **f,** Waters resolved in the core of the hNTSR1 receptor overlaid with the cryoEM map. **g,** Overlay of the hNTSR cryoEM structure (protein in green, SR48692 in purple) with the rNSTR-H4 crystal structure (protein in gray, SR48692 in pink) highlighting differences in ECL2.  **h,** Overlay of the hNTSR cryoEM structure (protein in green, SR48692 in purple) with the rNSTR-H4 crystal structure (protein in gray, SR48692 in pink) highlighting the residue shift and probable loss of bound water molecule caused by the F7.42V thermostabilizing mutation **i,** Overlay of the hNTSR cryoEM structure (protein in green, SR48692 in purple) with the rNSTR-H4bmx crystal structure (protein in gray, SR48692 in pink)

153    SR48692 (2.64 Å, 2.70 Å) or SR142948A (2.92 Å), which are small molecules previously

154    in development for treating cancer. Obtaining these structures required extensive

155    engineering to facilitate protein crystallization, with that work employing a construct of rat

156    NTSR1 evolved in bacteria to acquire numerous thermostabilizing mutations and fused

157    in TM7 with a DARPin[18] protein domain to facilitate crystal packing (rNTSR1-H4),

158    although a structure was also obtained with a back-mutated construct (rNTSR1-H4bmx)

159    at several positions to attempt to visualize a more native state[19]. To assess and compare

160    the cryo-EM/Nb6 approach with crystallography we obtained the cryo-EM structure of

161    hNTSR1/Nb6 complex bound to SR48692 (Fig. 2a, Extended Data Fig. 2). Notably, the

162    cryo-EM structure was resolved at a global resolution of 2.4 Å, both a higher nominal

163    resolution than the crystal structure and with better-resolved features, including the

164    density corresponding to the ligand (Fig. 2a-e, Extended Data Fig. 3a, 3b, 8a). This

165    resolution range also reveals densities corresponding to extensive hydration throughout

166    the receptor in the cryo-EM map (Fig. 2f, Extended Data Fig. 3c).

167        The construct for hNTSR1 was minimally modified beyond the KOR ICL3 swap,

168    with only N- and C- termini truncations in regions not resolved in typical family A structures

169    and a single A85$^{1.54}$L mutation to increase expression[20]. While the general ligand pose is

170    very similar, the cryo-EM structure reveals additional interactions not observed in the

171    rNTSR-H4 and/or rNTSR-H4bmx crystal structures. First, remodeling of the TM7-ECL3

172    region allows W334 in ECL3 to be fully resolved in the hNTSR1 structure loosely capping

173    the top of the hydrophobic chloro-naphthyl and dimethoxy-phenyl moieties of SR48692

174    (Fig. 2g). This change may be due to several amino acid sequence differences at the top

175    of TM7, most prominently P336$^{7.25}$ in hNTSR1 versus T341$^{7.25}$ in rNTSR1, with the proline

176 inducing a sharp turn between the top of TM7 and ECL3 in hNTSR1. In addition, a

177 rearrangement of R327$^{6.54}$ in rNTSR-H4 (R322$^{6.54}$ in hNTSR1) appears to disrupt a water-

178 mediated interaction between R327$^{6.54}$, R328$^{6.55}$ (R323$^{6.55}$ in hNTSR1), and the

179 carboxylate moiety of SR48692 observed in the hNTSR1 structure (Fig. 2h). This R327$^{6.54}$

180 rearrangement likely stems from the F358$^{7.42}$V thermostabilizing mutation in rNTSR-H4,

181 allowing a downward relaxation of Y324$^{6.51}$ (Y319$^{6.51}$ in hNTSR1) and R327$^{6.54}$. This water

182 molecule is also displaced in the rNTSR-H4bmx structure due to a different

183 rearrangement of R327$^{6.54}$ and R328$^{6.55}$, likely resulting from a shift in the W321$^{6.48}$

184 rotamer not observed in either hNTSR1 or rNTSR-H4bmx (Fig 2i). Notable differences

185 also exist in the TM helices between the two structures; TM1 is shifted with respect to the

186 core of the receptor in both crystal structures in varying degrees and directions (Extended

187 Data Fig. 3d). In addition, the top of TM2 and ECL1 are out of register by one residue

188 between hNTSR1 and rNTSR-H4. While this may be due to the differences in

189 experimental constructs, the observed discrepancy may also result from the fact that even

190 at σ=1 the 2Fo-Fc map of the crystal structure lacks sidechain information in the ECL1

191 region, rendering modeling ambiguous (Extended Data Fig. 3e,f). Overall, the lack of

192 thermostabilizing mutations and DARPin in TM7 restores a more native-like inactive state

193 as suggested by the conformation of key amino acids. For example, Y364$^{7.53}$ of the

194 hNTSR1 NPxxY motif (Y369$^{7.53}$ in rNSTR1) occupies a position and rotamer more typical

195 of an inactive state family A GPCR (Extended Data Fig. 3g).

196

197 **Structure of MOR**

198    Using the same approach, we obtained a cryo-EM structure of the MOR bound to

199    the non-blood brain barrier penetrant, MOR selective inverse agonist alvimopan, an FDA-

200    approved drug for reversing opioid-induced gastrointestinal (GI) symptoms in hospital

201    settings. In the case of NTSR1/Nb6, vitrifying the sample in a very thin buffer layer on

202    holey gold grids[21] was necessary for high resolution and to achieve proper alignment of

203    particle projections. To assess an alternative approach, we used Nb6 to develop a

204    megabody, termed 'Mb6', a fusion of a nanobody and a scaffold protein of either 45 or 86

205    kDa that can serve as a larger fiducial marker, based on the work of Uchański *et al.*[6]. In

206    that work, the Mb designs employed for GABA$_A$ and WbaP resulted in cryo-EM maps that

207    could not resolve well past the nanobody portion, presumably due to flexibility. We thus

208    opted instead for using the c7HopQA12 design, which incorporates a twisted linker

209    between the nanobody and the 45 kDa HopQ scaffold to increase their contact and,

210    ideally, rigidity. However, our MD simulations suggested that even this design was

211    characterized by substantial flexibility between the Nb and scaffold (Extended Data Fig.

212    5a). In agreement with this result, our cryo-EM 2D class averages of the MOR-Mb6

213    complex showed that only the Nb6-receptor portion is well resolved, with the scaffold

214    averaging out (Extended Data Fig. 4b). Nevertheless, leveraging the ordered Nb6 portion

215    of Mb6 in our cryo-EM data, we obtained a 2.8 Å cryo-EM map (Fig. 3a, Extended Data

216    Fig. 4) with unambiguous density for the ligand and receptor (Fig. 3c, Extended Data Fig.

217    8b). This level of detail is quite comparable to the 2.8 Å crystal structure of MOR (Fig. 3b,

218    d), although the cryo-EM map further resolves several probable water molecules in the

219    ligand binding site, including one that bridges interactions between the carboxylate of

220    alvimopan and the receptor (Extended Data Fig. 5b).

221        Comparing the binding poses of the MOR-selective alvimopan with that of the

222    structurally similar ligand JDTic, which is selective for KOR, reveals a striking difference.

223    Despite their similar scaffolds, the phenol-piperidine moieties of alvimopan and JDTic are

224    in completely different positions and orientations, nearly flipped in the binding pocket.

225    Aligning our structure with KOR-JDTic (PDB:4DJH[22]) reveals that JDTic would clash with

226    Y326$^{7.43}$ and Q124$^{2.60}$ in MOR, while alvimopan would clash with W124 and I294$^{6.55}$ in
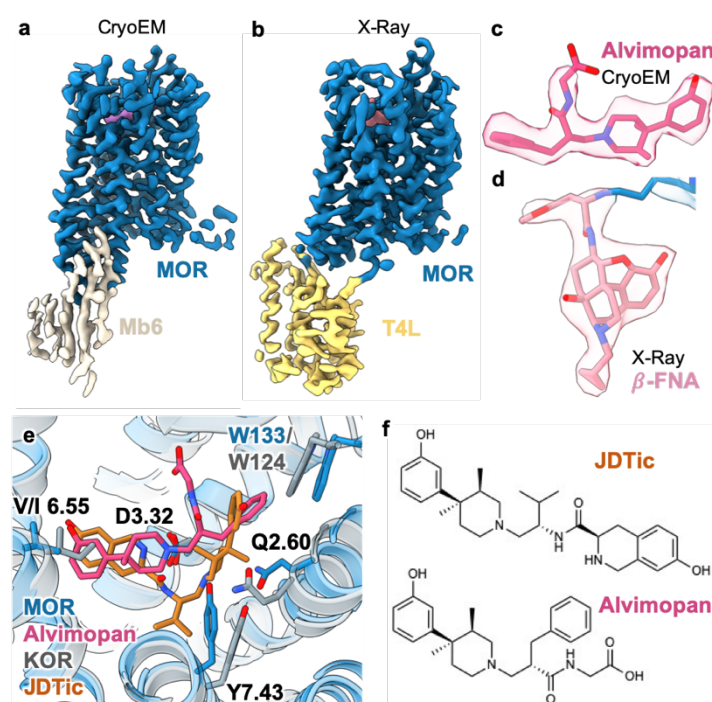


**Fig 3. Comparison of cryo-EM structure of alvimopan-bound MOR with crystal structures of MOR/β-FNA and KOR/JDTic**
**a,** Cryo-EM map of MOR at 2.8 Å global resolution. **b,** 2Fo-Fc crystallography map of MOR at 2.8 Å contoured at $\sigma$=2.0. **c,** Cryo-EM density and model for inverse agonist alvimopan. **d,** Local 2Fo-Fc map around β-FNA contoured at $\sigma$=1.5. **e,** overlay of the alvimopan pose in the MOR cryo-EM structure (protein in blue, alvimopan in magenta) with the JDTic pose in the KOR crystal structure (protein in grey, JDTic in orange). **f,** Comparison of JDTic and alvimopan chemical structures highlighting similar phenol-piperidine scaffold.

227    KOR (I294$^{6.55}$ of KOR is substituted by a repositioned valine in MOR). In addition to the

228    steric confines of the binding pocket, charge differences also appear to contribute to the

229    differences in binding pose between JDTIC and alvimopan. The nitrogen of the

230    tetrahydroisoquinoline ring system of JDTic is likely also protonated or perhaps

231    protonated instead of the piperidine, and thus forms salt bridge interactions with D138$^{3.32}$

232    (D147$^{3.32}$ in MOR), just as the protonated piperidine of alvimopan does in MOR. Of note,

233    alvimopan shares similarities to fentanyl and its analogues, including a central piperidine

234   ring. Computational docking of carfentanil[23], a potent MOR agonist, in the active-state

235   structure of the receptor[3] suggests a pose similar to alvimopan, but with the additional

236   phenylamine moiety on the piperidine ring positioned to bind into the pocket occupied by

237   the toggle switch tryptophan W293[6.48] (Extended Data Fig. 5a). How a MOR ligand

238   engages this region is often the main determining factor for its agonism versus

239   antagonism. Based on our observations, we hypothesize that this phenyl moiety of

240   fentanyl and its derivatives is responsible for converting the piperidine scaffold to an

241   agonist.

242

243   **Structure of SSTR2**

244        To test the cryo-EM/Nb6 approach on a receptor without prior structural

245   characterization we chose SSTR2, a member of the SSTR subfamily for which no

246   structures have been determined. Despite the absence of a stabilizing inverse agonist or

247   any other ligand, and not using an energy filter for cryo-EM data acquisition (typically

248   beneficial for improved contrast when imaging small proteins), we were able to obtain a

249   3.1 Å map of SSTR2/Nb6 with well-resolved features (Fig. 4a, Extended Data Fig. 6, 8c).

250   Together with two active-state structures of SSTR2 bound to two different agonists, the

251   endogenous 14-mer SST14 and the synthetic 8-mer octreotide[24], the inactive-state

252   SSTR2 structure enabled us to characterize several aspects of receptor activation and

253   ligand recognition. Perhaps the most interesting feature of SSTR2 is the conformational

254   flexibility of ECL2; while in a well-defined position in the apo state structure, ECL2 is

255   pushed to a more open conformation when bound to the endogenous agonist SST14, but

256   folds down over the top of the receptor in the octreotide-bound state (Fig. 4b). As a

257   consequence of the ECL2 plasticity, different residues are engaged in binding the pan-

258   SSTR agonist SST14 versus the SSTR2-selective octreotide. This is an important factor

259   to SSTR subtype selectivity, which is explored further in our recent study[24].

260       Very few structures have been obtained to date for family A GPCRs in the

261   unliganded, apo state, primarily due to the general need for a stabilizing ligand to obtain

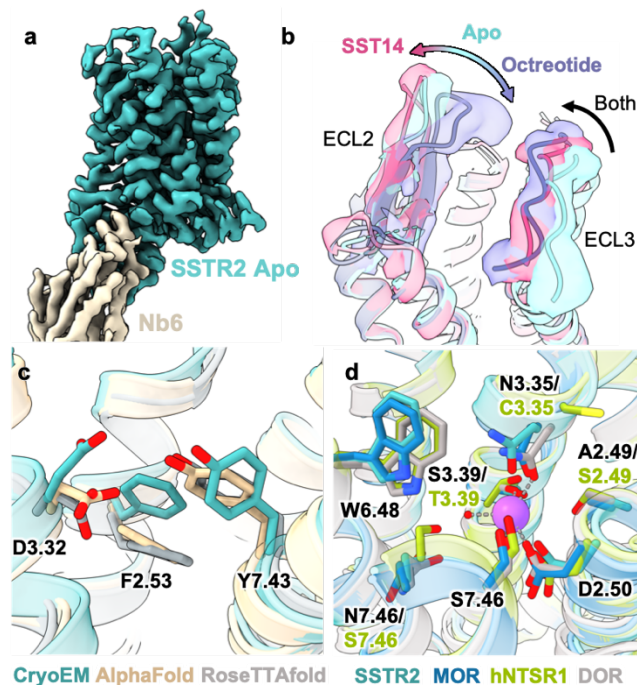262   a crystal structure. Experimentally-derived apo structures provide an opportunity to



**Fig 4. | Cryo-EM structure of the apo SSTR2 and comparison of sodium ion binding site.**
**a,** Cryo-EM map of SSTR2 at 3.1 Å global resolution. **b,** Comparison of the model and cryo-EM maps of apo SSTR2 (teal) and SSTR2 in complex with either SST14 (magenta) or octreotide (purple). **c,** Comparison of the CryoEM structure of SSTR2 (teal) with AlphaFold (tan) and RoseTTAfold (gray) predictions. **d,** Overlay of SSTR2 (teal), MOR (blue), and NTSR1 (green) cryo-EM structures around the canonical family A sodium ion binding site with the DOR sodium coordination site structure (gray, PDB:4N6H).

263   evaluate predicted structures from the recently published deep-learning based tools,

264   AlphaFold2[25] and RoseTTAfold[26]. Notably, while both software performed well in

265   predicting the overall structure of SSTR2, key details of the ligand binding site were in

266   disagreement with the experimental structure, particularly in residues D122$^{3.32}$, F92$^{2.53}$,

267   and Y302$^{7.43}$ (Fig. 4c), which are involved in ligand binding and activation, as detailed in

268   the companion active-state SSTR2 manuscript[24]. Although a more systematic

269   comparison is needed, this observation underscores both the merits and the potential

270   limitations of homology model-based approaches. Differences in side chain positioning,

271    especially within a ligand binding site, can throw off structure-based drug discovery efforts

272    and other pursuits requiring high-accuracy coordinates.

273

274    **Differential sodium accommodation by family A GPCRs**

275         Our near-native inactive-state cryo-EM maps provide the opportunity to examine

276    the allosteric sodium binding site found deep in the core of many family A receptors. For

277    NTSR1, MOR, and SSTR2 there is strong experimental evidence for negative allosteric

278    modulation by sodium[27–29]. In both MOR and SSTR2, the identities of the residues in the

279    sodium binding site are the same as the δ-opioid receptor (DOR), for which there is a

280    high-resolution crystal structure (1.8 Å) with a well-defined sodium site[30] (Fig. 4c). The

281    geometries of the MOR, SSTR2, and DOR sites are very similar, with the exception of a

282    slight rearrangement of $W^{6.48}$ in the case of both MOR ($W293^{6.48}$) and SSTR2 ($W269^{6.48}$),

283    and $N125^{3.35}$ in SSTR2. In contrast to SSTR2 and MOR, hNTSR1 has four amino acid

284    differences in the sodium binding site, namely $T155^{3.39}$ (in place of $S^{3.39}$), $S357^{7.46}$ (in

285    place of $N^{7.46}$), $S111^{2.49}$ (in place of $A^{2.49}$), and $C151^{3.35}$ (in place of $N^{3.35}$). In the DOR

286    structure, both $S135^{3.39}$ and $N131^{3.35}$ directly interact with the sodium.

287         The three maps we determined resolve features consistent with water and/or ions

288    in the canonical sodium binding region near $D^{2.50}$, although only NTSR1 has sufficiently

289    high resolution in this region to facilitate unambiguous ion modeling (Extended Data Fig.

290    7a-c). The probable ion sites of SSTR2 and MOR match relatively well to those observed

291    in DOR. In the hNTSR1 map, we observe a density with close proximity to oxygen atoms

292    of $T155^{3.39}$, $S111^{2.49}$, $D112^{2.50}$ (Extended Data Fig. 7a). Even though precise identification

293    of water versus ion is challenging in cryo-EM maps, we expect that this feature

294    corresponds to the sodium, shifted by 1.8 Å compared to the sodium in DOR (Fig. 4d,

295    Extended Data Fig. 7d, e). As other receptors with resolved sodium ion sites have

296    cysteine or other hydrophobic residues in place of $N^{3.35}$, $S111^{2.49}$ is likely responsible for

297    the shift in sodium position in NTSR1. Overall, we find substantial similarity between the

298    sodium binding sites of inactive state GPCRs from cryo-EM and crystallography.

299

300    **Structural Basis of Histamine Receptor Subtype Selectivity**

301         Notwithstanding the success of Nb6 alone to obtain these structures, we sought to

302    generate a larger, rigid Nb6-based fiducial that would enable the alignment of potentially

303    more challenging targets and also extend this approach to less powerful electron

304    microscopy platforms. To this end we generated an 'alpacaized' Nb6 where the antigen

305    binding loops of Nb6 were grafted onto an alpaca nanobody scaffold[8]. This modified Nb6,

306    called Nb6M, was used to bind H2R possessing the KOR ICL3 swap in complex with the

307    FDA approved H2 blocker famotidine. The complex was additionally decorated with a

308    NabFab[8] (a Fab antibody fragment that binds alpaca nanobodies) and an anti-Fab

309    nanobody that has been shown to reduce Fab flexibility[31]. The structure of the entire

310    complex was determined by cryo-EM at a global nominal resolution of 3.0 Å (Fig. 5a,

311    Extended Data Fig. 8). With the exception of the anti-Fab nanobody, the structure is well

312    resolved, with local refinement on the receptor and Nb6M region further enhancing the

313    details of H2R and bound famotidine (Fig. 5b, Extended Data Fig. 8e). Notably, a lipid

314    molecule can be observed wedged between TM1 and TM7 and interacting with $Q79^{2.62}$,

315    in a similar position observed previously in cryoEM maps with certain family A GPCRs[32]

316    although its role remains unclear (Extended Data Fig. 9a).

317     Comparing our cryo-EM structure of H2R/famotidine with the crystal structure of

318     H1R bound to the H1R selective doxepin (PDB:3RZE[33]) reveals clearly the structural

319     basis for subtype selectivity between H1R and H2R. H1R ligands, including  the FDA

320     approved doxepin, loratadine, and cetirizine (Extended Data Fig. 9b-d) possess a distinct

321     diphenyl group that occupies a large hydrophobic pocket in H1R comprised of $W^{4.56}$, $F^{6.55}$,

322     $F^{6.52}$, and $Y^{3.33}$ (Fig. 5c). These compounds also include a single amine which is

323     protonated at neutral pH and interacts with the key aminergic aspartate $D^{3.32}$ present in

324     many family A GPCRs. The hydrophobic pocket where the diphenyl moiety binds in H1R

325     is substantially perturbed in H2R, with the substitution of $Y^{3.33}V$ and repositioning of $W^{4.56}$

326     in H1R with $S^{4.57}$ in H2R removing major hydrophobic and pi-pi interaction partners (Fig.

327     5c). Further, TM6 shifts inward, repositioning $F^{6.55}$ and $F^{6.52}$ and resulting in a partial

328     closure of the pocket (Fig. 5c). Several additional residues, including $C^{3.36}$ ($S^{3.36}$ in H1R)

329     occupy rotamers in the famotidine-bound state that would sterically clash with doxepin

330     binding.
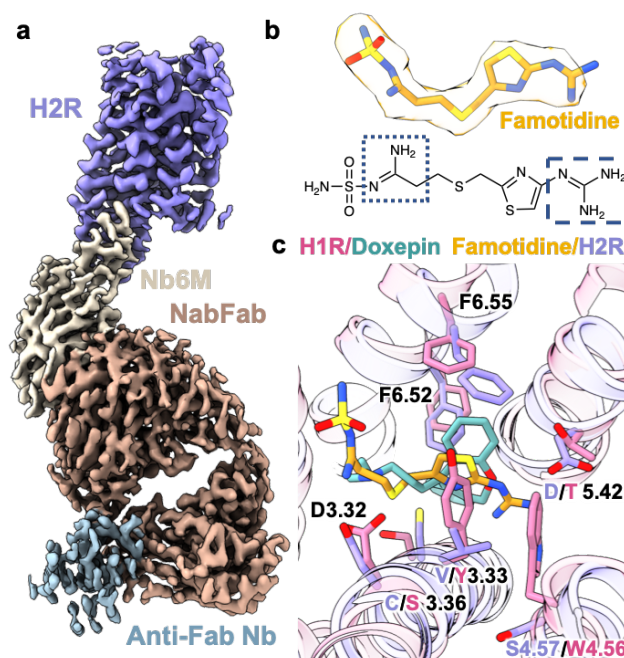


**Fig 5. Cryo-EM structure of the H2R/Famotidine/Nb6M/NabFab/Anti-Fab complex and comparison to H1R/Doxepin**
**a,** 3.0 Å global resolution cryo-EM map of inactive-state H2R complex. **b,** Famotidine in the cryo-EM density and chemical schematic; protonatable amine groups are boxed in blue, with the moiety protonated near neutral pH on the right in large dashed lines, and the moiety likely protonated at low pH on the left in small dotted lines. **c,** Overlay of H1R (magenta) and doxepin (teal) crystal structure with the H2R (lavender) and famotidine (gold) cryo-EM structure.

331        Famotidine and doxepin differ in their chemical structures, where famotidine is a

332      primarily linear molecule with two amine-containing moieties (Fig. 5b), a common feature

333      of H2R blockers (Extended Data Fig. 9e-g). These two amine-containing groups of H2R

334      antagonists tend to differ substantially in their pKas, with one that is likely protonated at

335      or near pH 7.0 (the guanidine group in the case of famotidine, Fig. 5b; dashed lines) and

336      a second that would require a far lower pH for protonation (the amidine/thiazole region

337      for famotidine[34], Fig. 5b, dotted lines). However, as H2R antagonists are primarily used

338      for diseases of gastric acid and bind to hydrochloric acid-secreting parietal cells, the

339      precise protonation state in the therapeutic environment is difficult to predict. Regardless

340      of protonation state, the binding pose is likely very similar; the protonated high-pKa amine

341      moiety forms a salt bridge with $D^{5.42}$ while the other amine-containing group interacts with

342      $D^{3.32}$ via either hydrogen bonding or a salt bridge (Fig. 5c). Prior functional studies have

343      also suggested that $D^{5.42}$ is a main determinant in subtype selectivity for H2R blockers[35],

344      with this position corresponding to a threonine in H1R, which is unable to form the key

345      salt bridge. Our docking studies with the other FDA approved H2R blockers cimetidine

346      and ranitidine suggest this 'di-aminergic' ligand binding at H2R is a common feature of

347      H2R antagonists (Extended Data Fig. 9e-g). Additional factors contributing to the lack of

348      binding of famotidine to H1R include the steric clash with $W^{4.54}$ (S in H2R) and the

349      modulation of the shape of the hydrophobic binding pocket (Fig. 5c).

350

351      **Discussion**

352         Here, we present inactive-state structures of four family A GPCRs, all obtained by

353      cryo-EM at resolutions as high as 2.4 Å by employing minimal engineering and a universal

354    nanobody for projection alignment. By using molecular dynamics simulations to assess

355    fiducial markers for use in cryo-EM structure determination, we could accurately predict

356    that Nb6 is sufficiently rigid for cryo-EM particle alignment, while Mb6 is too flexible for

357    resolution beyond the nanobody portion. Additionally, the enhanced decoration

358    opportunities afforded by the alpacaized Nb6M provide an additional tool for structure

359    determination of potentially more challenging targets and with less powerful cryo-EM

360    imaging set-ups such as those of 200kV and even 100kV. Each of the cryo-EM structures

361    described here yields new insights into ligand recognition, with resolution that is as good

362    or better than that of analogous structures produced by X-ray crystallography. In contrast

363    to active state GPCR-G protein complexes, where the highest-resolution portion of the

364    map is on the larger G protein due to the center of alignment, the inactive-state Nb6

365    GPCR structures display their highest resolution at the receptor core, facilitating accurate

366    modeling of ligands and their surrounding hydration. Even with the inclusion of NabFab,

367    local refinement on the receptor-Nb6M yielded a very well resolved ligand binding cavity.

368    This generalizable approach opens this broad family of drug targets to rapid,

369    crystallization-free structure determination, with biochemical stability of the receptor and

370    nanobody binding being the only limitations. As such, we anticipate Nb6 to be a broadly

371    applicable approach to determining inactive state structures of near-native GPCRs,

372    further propelling drug discovery in this class of receptors.

373

374    **Author Contributions**

375    M.J.R. cloned constructs, expressed and purified proteins, processed EM data, built

376    models, and ran/analyzed molecular dynamics simulations. M.P.S. expressed and

377    purified proteins and collected cryo-EM data. F.H. cloned constructs and expressed

378    proteins. J.M. performed BRET assays. A.S. prepared cryo-EM samples and collected

379    cryo-EM data. M.C. expressed proteins and purified nanobody. O.P. prepared cryo-EM

380    samples and collected cryo-EM data. T.C. provided constructs for nanobody expression

381    and BRET assays. M.J.R. and G.S. wrote the manuscript with input from M.P.S., F.H.,

382    J.M., O.P., and T.C.. G.S. supervised the project.

383

384    **Data Availability**

385    All data generated or analyzed in this study are included in this article and the

386    Supplementary Information. The cryo-EM density maps and corresponding coordinates

387    have been deposited in the Electron Microscopy Data Bank (EMDB) and the Protein Data

388    Bank (PDB), respectively, under the following accession codes: NTSR1 (EMD-26589,

389    PDB:7UL2), H2R (EMD-26590, PDB:7UL3), MOR (EMD-26591, PDB:7UL4), SSTR2

390    (EMD-26592, PDB:7UL5). Raw data has been deposited in EMPIAR under the following

391    accession codes:

392

393    **Competing Interests**

394    The authors declare no competing interests.

395

396    **Acknowledgements**

397    We thank the Kobilka lab for providing plasmids of NTSR1 and MOR. We thank the

398    Kossiakoff lab for providing the plasmid for NabFab and constructive feedback. Cryo-

399    EM data were collected at the Stanford cryo-EM center (cEMc) with support from E.

400    Montabana. This work was supported, in part, by the Mathers Foundation (G.S.),

401    training grant T32GM089626 (J.G.M.), the National Institute of Health R35GM143061

402    (T.C.), and used the Extreme Science and Engineering Discovery Environment

403    (XSEDE)[36] resource comet-gpu through sdsc-comet allocation TG-MCB190153 (G.S.),

404    which is supported by National Science Foundation grant number ACI-1548562.

405

406    **Methods**

407

408    **Cloning**

409    The cDNA for SSTR2 was obtained from Horizon Discovery and cloned into a pFastBac

410    vector containing an N-terminal haemagglutinin (HA) signal sequence followed by a FLAG

411    epitope (DYKDDDD) and a C-terminal C3 protease cleavage site followed by enhanced

412    green fluorescent protein (eGFP) and a hexahistidine (His6) tag using Gibson cloning.

413    Constructs for hNTSR1 and MOR were obtained from the lab of Brian Kobilka and have

414    been described previously[3,20]. Briefly, each is cloned in pFastBac with an N-terminal

415    haemagglutinin (HA) signal sequence followed by a Flag epitope (DYKDDDD) and a C-

416    terminal HRV 3C protease cleavage site followed by a hexahistidine (His6) tag. In the

417    case of hNTSR1, the His6 tag is preceded by enhanced green fluorescent protein (eGFP).

418    For MOR, two point mutations (M264L and K269R) were introduced with site-directed

419    mutagenesis; all PCR reactions were conducted with Q5 polymerase.

420    For hNTSR1, residues between T247$^{5.59}$ to L277$^{6.3}$ of kappa opioid were substituted,

421    for SSTR2, residues between S238 and K252 were replaced with those of kappa opioid

422    receptor, and for H2R residues from $V244^{5.56}$ to $V285^{6.46}$ were exchanged for kappa

423    opioid.

424    **Biolumescence resonance energy transfer (BRET) assays**

425    BRET assays were performed and analyzed as previously described[4] with the following

426    modifications: HEK-293S cells grown in FreeStyle 293 suspension media (Thermo

427    Fisher) were transfected at a density of 1 million cells/mL in 2 mL volume using 600 ng

428    total DNA at 1:1 ratio of Receptor-rLuc:Nb6-mVenus and a DNA:PEI ratio of 1:5,

429    and incubated in a 24 deep well plate at 220 rpm, 37°C for 48 hours. Cells were harvested

430    by centrifugation, washed with Hank's Balanced Salt Solution (HBSS) without

431    Calcium/Magnesium (Gibco), and resuspended in assay buffer (HBSS with 20 mM

432    HEPES pH 7.45) with 1 μg/mL freshly prepared coelenterazine h (Promega). Cells were

433    plated in white-walled, white-bottom 96 well plates (Costar) in a volume of 60 μl/well and

434    60,000 cells/well. Ligands were prepared in drug buffer (assay buffer with 0.1% BSA, 6

435    mM $CaCl_2$, 6 mM $MgCl_2$), and added at a 1:2 ratio of drug:cell suspension. Ten minutes

436    after the addition of ligand, plates were read using a SpectraMax iD5 plate reader using

437    485 nm and 535 nm emission filters with a one-second integration time per well. The

438    computed BRET ratios (mVenus/RLuc emission) were normalized to ligand-free control

439    (Net BRET) prior to further analysis.

440

441    **Expression and Purification of Nb6, Mb6, and Nb6M**

442    Wk6 *E. coli* (ATCC) were transformed via heat shock with Nb6 plasmid[4] and two 5 mL

443    starter cultures were grown overnight in LB supplemented with 100 μg/ml ampicillin. 2L

444    of terrific broth were supplemented with 100 μg/ml ampicillin, inoculated with starter

445    cultures, and grown at 37°C with shaking until OD$_{600}$=0.7. Expression was then induced

446    with 1mM IPTG and expression was allowed to proceed at 28°C overnight. Pellets were

447    harvested via centrifugation and washed once with phosphate-buffered saline before

448    snap freezing in liquid nitrogen. Pellets containing Nb6 were thawed and resuspended in

449    50 mM Tris pH 8.0, 0.5 mM EDTA, 20% w/v sucrose (TES) buffer at 15 mL / 1 liter pellet

450    and supplemented with protease inhibitor cocktail and shaken in an orbital shaker for 1

451    hour at 4°C. An additional 30 mL per 1 liter pellet of TES diluted 1:4 with water was added

452    and placed in an orbital shaker for an additional 45 minutes at 4°C. Cell debris was

453    removed by ultracentrifugation at 100,000xg for 30 minutes. The supernatant was filtered

454    with a 45 micron filter, supplemented with 20 mM imidazole, and loaded over a gravity Ni-

455    NTA column at 4°C. The column was washed with 10 CV of a buffer containing 250 mM

456    NaCl, 50 mM Tris pH 7.5, 10 mM imidazole, and then eluted with buffer containing 250

457    mM imidazole. Nanobody was concentrated and applied to size exclusion

458    chromatography with a buffer containing 250 mM NaCl and 50 mM Tris pH 7.5.

459    Monomeric fractions were pooled, concentrated, supplemented with 10% glycerol, and

460    snap frozen in liquid nitrogen for later use. Expression and purification of Mb6 and Nb6M

461    was performed identically to Nb6.

462

463    **Expression and Purification of NabFab**

464    Chemically competent C43 *E. coli* were transformed via heat shock with NabFab

465    plasmid[8]. A culture of 10 mL 2xYT media (16g/L tryptone, 10g/L yeast extract, 5g/L NaCl)

466    was inoculated with a single colony and incubated at 37°C with shaking overnight. TB

467    autoinduction media (Terrific Broth supplemented with 0.4% glycerol, 0.01% glucose,

468    0.02% lactose,1.25 mM MgSO$_4$, and 100 µg/ml ampicillin) was inoculated from starter

469    cultures and incubated for 6 hrs at 37 °C, 225 rpm, before decreasing the temperature to

470    30°C for overnight growth. The cells expressing NabFab were harvested by centrifugation

471    and snap-frozen in liquid nitrogen for storage. To purify NabFab, cell pellets were thawed

472    and resuspended in lysis buffer containing 20 mM sodium phosphate, pH 7.4, 150 mM

473    NaCl, DNaseI, and protease inhibitor cocktail), and lysed by sonication. The lysate was

474    then incubated at 63-65 °C for 30 minutes before centrifugation at 20,000 xg for 30

475    minutes. The supernatant was collected and run over a Protein G column pre-equilibrated

476    with 20 mM sodium phosphate, 500 mM NaCl, pH 7.4. The NabFab was then eluted with

477    0.1 M acetic acid and immediately loaded onto a Resource S cation exchange column

478    pre-equilibrated with buffer A (50 mM sodium acetate, pH 5.0). The column was washed

479    with 5 CV of buffer A and protein then eluted over a salt gradient 0-100% buffer B (50 mM

480    sodium acetate, 2M NaCl, pH 5.0). Eluted NabFab was dialyzed overnight into 150 mM

481    NaCl, 20 mM HEPES, pH 7.5 and then concentrated to 3 mg/mL for complexation.

482

483    **Expression and Purification of Receptor/Nb6 Complexes**

484    All receptors were expressed in Sf9 insect cells (Expression Systems) infected at a

485    density of 3-4 million cells/ml. At 48 hours post-infection, cells were collected with

486    centrifugation, washed with phosphate-buffered saline containing 10 µM antagonist

487    (when used), and pellets were snap frozen in liquid nitrogen for purification. A general

488    protocol was used for producing receptor/Nb6 complexes (Fig. S1), with some slight

489    deviations. Sf9 pellets containing receptor were lysed in hypotonic buffer containing 20

490    mM HEPES pH 7.5, 5 mM $MgCl_2$, protease inhibitor cocktail, benzonase, 10 $\mu$M

491    antagonist (when used), and 2 mg/ml iodoacetamide and gently stirred for an hour at 4°C.

492    Membranes were harvested with ultracentrifugation at 100,000xg, supernatant was

493    discarded, and membranes were resuspended in solubilization buffer containing 250 mM

494    NaCl, 20 mM HEPES pH 7.5, 1 mM $MgCl_2$, protease inhibitor cocktail, 10 $\mu$M antagonist

495    (when used), and 2 mg/ml iodoacetamide; then drip frozen into liquid nitrogen and stored

496    at -80°C. Resuspended membranes were thawed and detergent was added dropwise

497    while stirring at 4°C to a final concentration of 1% LMNG/0.1% CHS/0.1% Cholate. After

498    3 hours, insoluble debris was removed with ultracentrifugation at 100,000 g. Solubilized

499    receptor was supplemented with 20 mM imidazole and gravity loaded over a Ni-NTA resin

500    column. Columns were washed with 10 column volumes of buffer containing 250 mM

501    NaCl, 20 mM HEPES pH 7.5, 10 $\mu$M antagonist (when used), 20 mM imidazole, and 0.1%

502    LMNG/0.01% CHS and protein was eluted in buffer containing 250 mM NaCl, 20 mM

503    HEPES pH 7.5, 10 $\mu$M antagonist (when used), 250 mM imidazole, and 0.01%

504    LMNG/0.001% CHS. Receptor was then supplemented with 5 mM $CaCl_2$ and loaded onto

505    M1 flag resin; washed with 5 column volumes of 250 mM NaCl, 20 mM HEPES pH 7.5,

506    10 $\mu$M antagonist (when used), 2 mM CaCl2, and 0.1% LMNG/0.01% CHS; and eluted

507    with buffer containing 150 mM NaCl, 20 mM HEPES pH 7.5, 10 $\mu$M antagonist (when

508    used), 1 mM EDTA, 0.2 mg/ml FLAG peptide, and 0.1% LMNG/0.01% CHS. Purified

509    receptor was incubated on ice overnight with HRV 3C protease and purified Nb6 was

510    added at a 2:1 molar ratio. Receptor/Nb6 complex was concentrated in a 50 kDa

511    molecular weight cutoff spin concentrator and subjected to SEC chromatography with an

512    ENrich 650 column (Bio-Rad) and a buffer containing 150 mM NaCl, 20 mM HEPES pH

513    7.5, 0.001% LMNG, 0.00033% GDN, and 0.0001% CHS. Fractions containing monomeric

514    receptor/Nb6 complex were pooled for cryo-EM sample preparation. This protocol was

515    identical for SSTR2, NTSR1, and H2R with the exception of the addition of 100 $\mu$M TCEP

516    to the lysis buffer for NTSR1 and incubation with Nb6M, NabFab, and anti-Fab Nb

517    (Thermo Fisher Scientific 1033270500) in the case of H2R. Preparation of MOR/Mb6

518    complex was identical to that of receptor Nb6 complex, with the omission of the HRV-3C

519    cleavage to remove eGFP as it was not present in the construct.

520

521    **Cryo-EM Sample Preparation**

522    All samples were prepared on glow-discharged holey gold grids (Quantifoil ultrAufoil

523    R1.2/1.3), blotted in a FEI Vitrobot Mark IV (Thermo Fisher Scientific) at 4°C and 100%

524    humidity, and plunge frozen into liquid ethane. Blotting conditions for each sample were

525    as follows: 3.0 $\mu$l of NTSR1/Nb6 complex at 16 mg/ml with an additional 0.05% beta OG;

526    3.0 $\mu$l of MOR/Mb6 complex at 5 mg/ml; 2.5 $\mu$l of SSTR2/Nb6 complex at 16 mg/ml with

527    an additional 0.05% beta OG; and 3.0 $\mu$l of H2R/Nb6M/NabFab/anti-Fab Nb at 2.5-4

528    mg/ml.

529

530    **Cryo-EM Data Collection**

531    All samples were collected on a KRIOS electron microscope at an accelerating voltage

532    of 300 kV, with an energy filter for NTSR1/Nb6, H2R/Nb6M/NabFab/anti-Fab Nb, and

533    MOR/Mb6 and without an energy filter for SSTR2/Nb6. All data was collected through

534    SerialEM with beam tilt compensation and recorded on a Gatan K3 direct electron

535    detector. The resulting image stacks have a pixel size of 0.434 Å for NTSR1/Nb6,

536    H2R/Nb6/NabFab, MOR/Mb6, and H2R/Nb6M/NabFab/anti-Fab Nb; and 0.426 Å for

537    SSTR2/Nb6, all in super resolution mode. Each NTSR1/Nb6 image stack is composed of

538    71 frames with an incident electron dose of 0.85 e$^-$/Å$^2$ per frame, for a total dose of 61 e$^-$

539    /Å$^2$/s per micrograph. Each MOR/Mb6 image stack is composed of 63 frames with an

540    incident electron dose of 0.98 e$^-$/Å$^2$ per frame, for a total dose of 61 e$^-$/Å$^2$/s per micrograph.

541    Each SSTR2/Nb6 image stack is composed of 55 frames with an incident electron dose

542    of 1.26 e$^-$/Å$^2$ per frame, for a total dose of 69 e$^-$/Å$^2$/s per micrograph. Each

543    H2R/Nb6M/NabFab/anti-Fab Nb image stack is composed of 68 frames with an incident

544    electron dose of 0.86 e$^-$/Å$^2$ per frame, for a total dose of 58.58 e$^-$/Å$^2$/s per micrograph.

545

546    **Cryo-EM Data Processing**

547    A pictorial depiction of each cryoEM processing workflow can be found in Figs. S2C, S4C,

548    S6C, and S8C. Briefly, dose-fractionated image stacks were imported into RELION-3.1[37]

549    and subjected to beam-induced motion correction and dose weighting with MotionCor2[38].

550    Contrast transfer function parameter estimation was performed with CTFFIND-4.1[39].

551    Particle selection and extraction was performed with the Laplacian autopicker function of

552    RELION-3.1 on micrographs with a CTF fit better than 3.5 Å. The extracted particle stack

553    was imported into CryoSPARC[40] and subjected to multiple rounds of 2D classification

554    followed by iterative rounds of *ab initio* reconstruction with multiple classes and

555    heterogeneous refinement to further classify particles. In early 3D iterations, particles

556    from poor 3D classes were subjected to additional 2D classification and good particles

557    were 'rescued' for further 3D classification. Once iterative *ab initio* and heterogenous

558    refinement no longer produced higher resolution reconstruction, particles were re-

559    imported to RELION-3.1. In the cases of hNTSR1 and MOR CTF fit cutoffs of 3.1 Å and

560    3.3 Å were applied, respectively. Particles were then subjected to 3D refinement in

561    RELION-3.1 followed by Bayesian polishing. Polished particles were then imported back

562    to CryoSPARC for non-uniform refinement, global CTF refinement based on optics group,

563    and repeated non-uniform and local refinement.

564

565    **Model Building and Refinement**

566    All initial models were rigid body fit into cryo-EM maps using the ChimeraX[41] software.

567    For hNTSR1, the cryo-EM model of active state hNTSR1 was used as the initial model

568    (PDB:6OS9[19]); for MOR the crystal structure of inactive MOR bound to a covalent

569    antagonist was used as the initial model (PDB:4DKL[42]), for SSTR2 a homology model

570    generated from KOR (PDB:6VI4[4]) was used; and for H2R a homology model generated

571    from H1R (PDB:3RZE[33]) was used. In all cases KOR/Nb6 complex (PDB:6VI4[4]) was

572    aligned to the receptor to produce the initial model for the nanobody. An initial structure

573    for the NabFab was taken from PDB:7PHP. All structures were manually refined in

574    COOT[43] with iterative real-space refinement in Phenix[44]. Once accurate modeling was

575    achieved for the protein components, the GemSpot pipeline[45] was used for automatic

576    modeling of the ligands alvimopan, SR48692, and famotidine into MOR, hNTSR1, and

577    H2R, respectively. Final refinement was executed in Phenix, followed by model-free

578    Phenix map modification for NTSR1 and MOR[46]. All maps displayed in this work are those

579    prior to model-free map modification unless stated otherwise.

580

581    **Molecular Dynamics Simulations**

582    Simulations of the KOR/Nb6 complex started with the crystal structure PDB:6VI4, with the

583    pose of JDTic replaced with that of PDB:4DJH[21]. Maestro's protein preparation tool was

584    used to assign protonation states, optimize hydrogen bonding, and build missing

585    sidechains and loops. Once the receptor was prepared, the orientation of proteins in

586    membranes webserver (OPM)[47] was used to align the receptor as it would be in a

587    membrane in the xy plane and the CHARMM-GUI[48] was used to build the full system with

588    a 1-palmitoyl-2-oleoyl-*sn*-glycero-3-phosphocholine POPC/CHS lipid bilayer, TIP3P

589    water[49], and 150 mM NaCl. PSF and PDB files were generated with the OPLS-AA/M[50,51]

590    forcefield in VMD[52] for the system. For Mb6, a homology model was built from PDB:6XVI

591    with the Prime homology modeling tool[53]. This model was solvated in TIP3P water and

592    150 mM NaCl in VMD for simulation.

593    Molecular dynamics simulations were carried out in NAMD[54] with a 2 fs timestep

594    with SHAKE and SETTLE algorithms[55,56], with a Langevin thermostat and a Nosé-Hoover

595    Langevin piston barostat at 1 atm with a period of 50 fs and decay of 25 fs. Periodic

596    boundary conditions were used with nonbonded interactions smoothed starting at 10 Å to

597    12 Å with long-range interactions treated with particle mesh Ewald (PME). The system

598    was minimized for 1,500 steps and then slowly heated from 0 to 303.15K in increments

599    of 20K simulating for 0.4 ns at each increment. For the Kappa/Nb6 simulations, all non-

600    hydrogen, non-water, and non-ion atoms were restrained with a 1 kcal/mol/ $Å^2$ harmonic

601    restraint during heating and an additional 10 ns of equilibration. 1 kcal/mol/ $Å^2$ harmonic

602    restraints were used for an additional 10 ns of equilibration on all non-hydrogen protein

603    atoms followed by a final 10 ns of restrained equilibration with 1 kcal/mol/ $Å^2$ harmonic

604    restraint on only C$\alpha$ atoms. The first 30 ns of unrestrained molecular dynamics were also

605 considered to be equilibration, with an additional 500 ns of simulation performed. All

606 simulations were performed in triplicate. For Mb6, the first 30 ns of unrestrained molecular

607 dynamics were treated as equilibration, and 100 ns of triplicate molecular dynamics

608 simulations were performed.

609

610 **Docking**

611 The cryo-EM structure of active MOR (PDB:6DDE)[3] was prepared in Maestro and

612 carfentanil was docked with Glide XP docking[57]. The cryo-EM structure of inactive H2R

613 was prepared in Maestro, and ranitidine and cimetidine were docked with Glide XP

614 docking[57]. The crystal structure of inactive H1R (PDB:3RZE) was prepared in Maestro

615 and loratadine and cetirizine were docked with Glide XP docking[57].

616

617 **References**

618 1.    Robertson, M. J., Meyerowitz, J. G. & Skiniotis, G. Drug discovery in the era of cryo-

619      electron   microscopy.   *Trends   in   Biochemical   Sciences*   (2021).

620      doi:10.1016/j.tibs.2021.06.008

621 2.    Hauser, A. S., Attwood, M. M., Rask-Andersen, M., Schiöth, H. B. & Gloriam, D. E. Trends

622      in GPCR drug discovery: New agents, targets and indications. *Nat. Rev. Drug Discov.*

623      (2017). doi:10.1038/nrd.2017.178

624 3.    Koehl, A. *et al.* Structure of the μ-opioid receptor-Gi protein complex. *Nature* **558**, 547–552

625      (2018).

626 4.    Che, T. *et al.* Nanobody-enabled monitoring of kappa opioid receptor states. *Nat. Commun.*

627      (2020). doi:10.1038/s41467-020-14889-7

628 5.    Gully, D. *et al.* Biochemical and pharmacological profile of a potent and selective

629      nonpeptide antagonist of the neurotensin receptor. *Proc. Natl. Acad. Sci. U. S. A.* (1993).

630    doi:10.1073/pnas.90.1.65

631    6.   Uchański, T. *et al.* Megabodies expand the nanobody toolkit for protein structure

632         determination by single-particle cryo-EM. *Nat. Methods* (2021). doi:10.1038/s41592-020-

633         01001-6

634    7.   Zimmerman, D. M. *et al.* Discovery of a Potent, Peripherally Selective trans-3,4-Dimethyl-

635         4-(3-hydroxyphenyl)piperidine Opioid Antagonist for the Treatment of Gastrointestinal

636         Motility Disorders. *J. Med. Chem.* (1994). doi:10.1021/jm00041a003

637    8.   Bloch, J., Mukherjee, S., Kowal, J., Filippova, E. V., Niederer, M., Pardon, E., Seyaert, J.,

638         Kossiakoff, A. A., Locher, K. P. Development of a universal nanobody-binding Fab module

639         for fiducial-assisted cryo-EM strudies of membrane proteins *P.N.A.S.* (2021)

640         doi:10.1073/pnas.2115435118

641    9.   Carraway, R. & Leeman, S. E. Characterization of radioimmunoassayable neurotensin in

642         the rat. Its differential distribution in the central nervous system, small intestine, and

643         stomach. *J. Biol. Chem.* (1976). doi:10.1016/s0021-9258(17)32938-1

644    10.  Christou, N. *et al.* Neurotensin pathway in digestive cancers and clinical applications: an

645         overview. *Cell Death and Disease* (2020). doi:10.1038/s41419-020-03245-8

646    11.  Liu, J. *et al.* neurotensin receptor 1 antagonist SR48692 improves response to carboplatin

647         by enhancing apoptosis and inhibiting drug efflux in ovarian cancer. *Clin. Cancer Res.*

648         (2017). doi:10.1158/1078-0432.CCR-17-0861

649    12.  Volkow, N. D. & Blanco, C. The changing opioid crisis: development, challenges and

650         opportunities. *Molecular Psychiatry* (2021). doi:10.1038/s41380-020-0661-4

651    13.  Volkow, N. D. & Collins, F. S. The Role of Science in Addressing the Opioid Crisis. *N. Engl.*

652         *J. Med.* (2017). doi:10.1056/nejmsr1706626

653    14.  Günther, T. *et al.* International union of basic and clinical pharmacology. CV. somatostatin

654         receptors: Structure, function, ligands, and new nomenclature. *Pharmacol. Rev.* (2018).

655         doi:10.1124/pr.117.015388

656    15.    Ballesteros, J. A. & Weinstein, H. Integrated methods for the construction of three-dimensional models and computational probing of structure-function relations in G protein-coupled receptors. *Methods Neurosci.* (1995). doi:10.1016/S1043-9471(05)80049-7

659    16.    Stoeber, M. *et al.* A Genetically Encoded Biosensor Reveals Location Bias of Opioid Drug Action. *Neuron* (2018). doi:10.1016/j.neuron.2018.04.021

661    17.    Deluigi, M. *et al.* Complexes of the neurotensin receptor 1 with small-molecule ligands reveal structural determinants of full, partial, and inverse agonism. *Sci. Adv.* (2021). doi:10.1126/sciadv.abe5504

664    18.    Mittl, P. R., Ernst, P. & Plückthun, A. Chaperone-assisted structure elucidation with DARPins. *Current Opinion in Structural Biology* (2020). doi:10.1016/j.sbi.2019.12.009

666    19.    Scott, D. J., Kummer, L., Egloff, P., Bathgate, R. A. D. & Plückthun, A. Improving the apo-state detergent stability of NTS1 with CHESS for pharmacological and structural studies. *Biochim. Biophys. Acta - Biomembr.* (2014). doi:10.1016/j.bbamem.2014.07.015

669    20.    Kato, H. E. *et al.* Conformational transitions of a neurotensin receptor 1–Gi1 complex. *Nature* **572**, 80–85 (2019).

671    21.    Russo, C. J. & Passmore, L. A. Ultrastable gold substrates for electron cryomicroscopy. *Science (80-. ).* (2014). doi:10.1126/science.1259530

673    22.    Wu, H. *et al.* Structure of the human κ-opioid receptor in complex with JDTic. *Nature* (2012). doi:10.1038/nature10939

675    23.    Van Bever, W. F. M., Niemegeers, C. J. E. & Schellekens, K. H. L. P. A. J. N 4 substituted 1 (2 arylethyl) 4 piperidinyl N phenylpropanamides, a novel series of extremely potent analgesics with unusually high safety margin. *Arzneimittel-Forschung/Drug Res.* (1976).

678    24.    Robertson, M. J., Meyerowitz, J. M., Panova, O., Borrelli, K. W., Skiniotis, G. Plasticity in Ligand Recognition at Somatostatin Receptors. *NSMB* (2022)

680    25.    Tunyasuvunakool, K. *et al.* Highly accurate protein structure prediction for the human proteome. *Nature* (2021). doi:10.1038/s41586-021-03828-1

682    26.    Baek, M. *et al.* Accurate prediction of protein structures and interactions using a three-track

683           neural network. *Science (80-. ).* (2021). doi:10.1126/science.abj8754

684    27.    Kong, H., Raynor, K., Yasuda, K., Bell, G. I. & Reisine, T. Mutation of an aspartate at

685           residue 89 in somatostatin receptor subtype 2 prevents Na+ regulation of agonist binding

686           but does not alter receptor-G protein association. *Mol. Pharmacol.* (1993).

687    28.    Martin, S., Botto, J. M., Vincent, J. P. & Mazella, J. Pivotal role of an aspartate residue in

688           sodium sensitivity and coupling to G proteins of neurotensin receptors. *Mol. Pharmacol.*

689           (1999). doi:10.1124/mol.55.2.210

690    29.    Yabaluri, N. & Medzihradsky, F. Regulation of μ-opioid receptor in neural cells by

691           extracellular sodium. *J. Neurochem.* (1997). doi:10.1046/j.1471-4159.1997.68031053.x

692    30.    Fenalti, G. DRUG DISCOVERY Molecular control of delta -opioid receptor signalling. *Nat.*

693           *-LONDON-* (2014).

694    31.    Ereño-Orbea J., Sicard T., Cui H., Carson J., Hermans P., Julien J.P. Structural Basis of

695           Enhanced Crystallizability Induced by a Molecular Chaperone for Antibody Antigen-Binding

696           Fragments *J. Mol. Biol.* (2018)

697    32.    Xu, P. *et al.* Structural insights into the lipid and ligand regulation of serotonin receptors.

698           *Nature* (2021) doi:10.1038/s41586-021-03376-8.

699    33.    Shimamura, I., *et al.* Structure of the human histamine H1 receptor complex with doxepin.

700           *Nature* (2011) doi:10.1038/nature10246.

701    34.    Marosi, A., Szalay, Z., Béni, S., Szakács, Z., Gáti, T., Rácz, Á., Noszál, B., Demeter, Á.

702           Solution-state NMR spectroscopy of famotidine revisited: spectral assignment, protonation

703           sites, and their structural consequences. *Anal. Bioanal. Chem.* (2021) doi:10.1007/s00216-

704           011-5599-6.

705    35.    Gantz, I., DelValle, J., Wang. L-D., Tashiro, T., Munzert, G., Guo, Y-J., Konda, Y., Yamada,

706           Y. Molecular Basis for the Interaction of Histamine with the Histamine H2 Receptor. *J. Biol.*

707           *Chem.* (1992) doi:10.1016/S0021-9258(19)36764-X.

708    36.    Towns, J. *et al.* XSEDE: Accelerating scientific discovery. *Comput. Sci. Eng.* (2014).

709            doi:10.1109/MCSE.2014.80

710    37.    Zivanov, J. *et al.* RELION-3: New tools for automated high-resolution cryo-EM structure

711            determination. *bioRxiv* (2018). doi:10.1101/421123

712    38.    Zheng, S. Q. *et al.* MotionCor2: Anisotropic correction of beam-induced motion for

713            improved cryo-electron microscopy. *Nature Methods* **14**, 331–332 (2017).

714    39.    Rohou, A. & Grigorieff, N. CTFFIND4: Fast and accurate defocus estimation from electron

715            micrographs. *J. Struct. Biol.* **192**, 216–221 (2015).

716    40.    Punjani, A., Rubinstein, J. L., Fleet, D. J. & Brubaker, M. A. CryoSPARC: Algorithms for

717            rapid    unsupervised    cryo-EM    structure    determination.    *Nat.    Methods*    (2017).

718            doi:10.1038/nmeth.4169

719    41.    Pettersen, E. F. *et al.* UCSF ChimeraX: Structure visualization for researchers, educators,

720            and developers. *Protein Sci.* (2021). doi:10.1002/pro.3943

721    42.    Manglik, A. *et al.* Crystal structure of the µ-opioid receptor bound to a morphinan

722            antagonist. *Nature* (2012). doi:10.1038/nature10954

723    43.    Emsley, P., Lohkamp, B., Scott, W. G. & Cowtan, K. Features and development of Coot.

724            *Acta Crystallogr. Sect. D Biol. Crystallogr.* **66**, 486–501 (2010).

725    44.    Adams, P. D. *et al.* PHENIX: A comprehensive Python-based system for macromolecular

726            structure solution. *Acta Crystallogr. Sect. D Biol. Crystallogr.* **66**, 213–221 (2010).

727    45.    Robertson, M. J., van Zundert, G. C. P., Borrelli, K. & Skiniotis, G. GemSpot: A Pipeline for

728            Robust    Modeling    of    Ligands    into    Cryo-EM    Maps.    *Structure*    (2020).

729            doi:10.1016/j.str.2020.04.018

730    46.    Terwilliger, T. C., Ludtke, S. J., Read, R. J., Adams, P. D. & Afonine, P. V. Improvement of

731            cryo-EM maps by density modification. *Nat. Methods* (2020). doi:10.1038/s41592-020-

732            0914-9

733    47.    Lomize, M. A., Pogozheva, I. D., Joo, H., Mosberg, H. I. & Lomize, A. L. OPM database

734      and PPM web server: Resources for positioning of proteins in membranes. *Nucleic Acids*

735      *Res.* **40**, (2012).

736   48.   Lee, J. *et al.* CHARMM-GUI Input Generator for NAMD, GROMACS, AMBER, OpenMM,

737      and CHARMM/OpenMM Simulations Using the CHARMM36 Additive Force Field. *J.*

738      *Chem. Theory Comput.* **12**, 405–413 (2016).

739   49.   Jorgensen, W. L., Chandrasekhar, J., Madura, J. D., Impey, R. W. & Klein, M. L.

740      Comparison of simple potential functions for simulating liquid water. *J. Chem. Phys.* **79**,

741      926–935 (1983).

742   50.   Robertson, M. J., Tirado-Rives, J. & Jorgensen, W. L. Improved Peptide and Protein

743      Torsional Energetics with the OPLS-AA Force Field. *J. Chem. Theory Comput.* **11**, 3499–

744      3509 (2015).

745   51.   Robertson, M. J., Skiniotis, G. Development of OPLS-AA/M Parameters for Simulations of

746      G-Protein Coupled Receptors and other Membrane Proteins. *bioRxiv.* (2022).

747   52.   Humphrey, W., Dalke, A. & Schulten, K. VMD: Visual molecular dynamics. *J. Mol. Graph.*

748      **14**, 33–38 (1996).

749   53.   Jacobson, M. P. *et al.* A Hierarchical Approach to All-Atom Protein Loop Prediction.

750      *Proteins Struct. Funct. Genet.* (2004). doi:10.1002/prot.10613

751   54.   Phillips, J. C. *et al.* Scalable molecular dynamics with NAMD. *Journal of Computational*

752      *Chemistry* **26**, 1781–1802 (2005).

753   55.   Ryckaert, J. P., Ciccotti, G. & Berendsen, H. J. C. Numerical integration of the cartesian

754      equations of motion of a system with constraints: molecular dynamics of n-alkanes. *J.*

755      *Comput. Phys.* (1977). doi:10.1016/0021-9991(77)90098-5

756   56.   Miyamoto, S. & Kollman, P. A. Settle: An analytical version of the SHAKE and RATTLE

757      algorithm for rigid water models. *J. Comput. Chem.* (1992). doi:10.1002/jcc.540130805

758   57.   Friesner, R. A. *et al.* Extra precision glide: Docking and scoring incorporating a model of

759      hydrophobic enclosure for protein-ligand complexes. *J. Med. Chem.* **49**, 6177–6196

760          (2006).

761